

1 Developing a rapid method for 3-dimensional
2 urban morphology detection using open-source
3 data

4 *Chao REN^a, Meng CAI^{b*}, Xinwei LI^a, Yuan SHI^b, Linda See^c*

5 ^aFaculty of Architecture, The University of Hong Kong

6 ^bSchool of Architecture, The Chinese University of Hong Kong, Shatin, N.T., Hong
7 Kong S.A.R., China

8 ^cInternational Institute for Applied Systems Analysis (IIASA), Laxenburg, Austria

9 **ABSTRACT**

10 Available and accessible three-dimensional (3D) urban morphology data have become
11 essential for extensive academic research on built-up environments and urban
12 climates. A rapid and consistent methodology for extracting urban morphology
13 information is urgently needed for sustainable urban development in global cities,
14 particularly given future trends of rapid urbanization. However, there is still a lack of
15 generally applicable methods that use open-source data in this context. In this study,
16 we developed a simple and highly efficient method for acquiring 3D urban
17 morphology information using open-source data. Building footprints were acquired
18 from the Maps Static application programming interface. Building heights were
19 extracted from an open digital surface model, i.e., the ALOS World 3D model with a
20 resolution of 30 m (AW3D30). Thereafter, urban morphological parameters, including

21 the sky view factor, building coverage ratio, building volume density, and frontal area
22 density, were calculated based on the retrieved building footprints and building
23 heights. The proposed method was applied to extract the 3D urban morphology of
24 Hong Kong, a city with a complex urban environment and a highly mixed
25 geographical context. The results show a usable accuracy and wide applicability for
26 the newly proposed method.

27 **KEYWORDS**

28 Urban morphology extraction; open-source data; open map service; morphological
29 parameters; satellite images.

30 **HIGHLIGHTS**

- 31 • A method was developed for the rapid acquisition of 3D urban morphology
32 information;
- 33 • Only open-source data and map services were used;
- 34 • The proposed method has a simple, high-efficiency workflow;
- 35 • The urban morphology of a complex city was detected using the proposed
36 method;
- 37 • The validation results show a usable accuracy and wide applicability.

38 **NOMENCLATURE**

3D

3-Dimensional

LiDAR	Light Detection and Ranging
SAR	Synthetic Aperture Radar
InSAR	interferometric Synthetic Aperture Radar
DSM	Digital Surface Model
OSM	OpenStreetMap
API	Application Programming Interface
GSV	Google Street View
DEM	Digital Elevation Model
BCR	Building Coverage Ratio
BVD	Building Volume Density
FAD	Frontal Area Density
SRTM	Shuttle Radar Topography Mission
ASTER GDEM	the Advanced Spaceborne Thermal Emission and Reflection Radiometer Global Digital Elevation Model
ALOS	Advanced Land Observing Satellite
AW3D30	Advanced Land Observing Satellite World 3D – 30m
BH	Building height
nDSM	normalized DSM
WRF	Weather Research and Forecasting

39

40 **1 INTRODUCTION**

41 Unprecedented growth in the global population has been observed in recent decades,
42 and 55% of the world’s population is now estimated to live in urban areas (UN
43 DESA, 2018). The United Nations also predicts that the global population growth
44 between 2012 and 2050 will occur mainly in cities, with close to 90% of this increase
45 taking place in urban areas in developing countries (UN DESA, 2015, 2018). The

46 continual construction associated with urban sprawl has resulted in profound urban
47 form changes, especially in less-developed countries and regions. Urban morphology
48 includes the urban form of individual buildings, open spaces, streets, and their
49 positions in relation to each other. Changes in urban morphology could lead to many
50 social, economic and environmental problems, such as increasing concentrations of
51 the population, traffic jams, housing shortages, resource shortages, biodiversity
52 reductions, “heat island” effects, noise, and air and water pollution (Cionco &
53 Ellefsen, 1998; Johansson, 2006; Lau, Chung, & Ren, 2019; Edward Ng, Yuan, Chen,
54 Ren, & Fung, 2011; Nichol, 1996; Wang et al., 2019; Wong et al., 2011; Yu, Liu, Wu,
55 & Lin, 2009). A sustainable urban environment can help mitigate or eliminate these
56 problems, and urban morphology information can provide fundamental data for
57 sustainable urban development in urban planning, construction, transportation, energy
58 and property management, environmental exposure, and so on (Suveg, 2004; Shearer
59 et al., 2006; Diamantini & Zanon, 2000). Therefore, a rapid and consistent
60 methodology for acquiring urban morphological data is paramount for developing
61 sustainable environments for cities, especially those subject to rapid urbanization that
62 also suffer from a lack of urban data.

63 However, generally applicable methods for using open-source data in cities
64 worldwide are still deficient. Field surveys have been used to collect 3D urban
65 morphology for years. However, although field surveys can be conducted to measure
66 the footprints and heights of buildings, they are often labor intensive and time
67 consuming, and only limited urban areas can be covered by conventional ground

68 surveys. Field measurements are also prone to sampling errors, especially when
69 volunteer-based personnel or those who are not experts are involved in the data
70 collection (Nowak, Hirabayashi, Bodine, & Greenfield, 2014).

71 Satellite image-based methods for the extraction of urban morphology have been
72 addressed by many researchers. Compared with conventional manual methods,
73 satellite-based technologies are fast and economical at obtaining urban morphological
74 information over large areas. Various remotely sensed data have been used to derive
75 urban information, including optical images (Paparoditis, Cord, Jordan, & Cocquerez,
76 1998; Shufelt, 1999; Turker & Koc-San, 2015; Hao, Zhang & Cao, 2016) and
77 synthetic aperture radar (SAR) (Paolo Gamba, Houshmand, & Saccani, 2000; He,
78 Jäger, Reigber, & Hellwich, 2008; Simonetto, Oriot, Garello, & Le Caillec, 2003),
79 Light Detection and Ranging (LiDAR) (Rottensteiner & Briese, 2002; Verma, Kumar,
80 & Hsu, 2006; Zhou & Neumann, 2008; Shan & Sampath, 2017), and interferometric
81 SAR (InSAR) data (Burkhart et al., 1996; Gamba et al., 2000; Luckman & Gray,
82 2003; Thiele, Cadario, Schulz, Thonnessen, & Soergel, 2007; Dubois, Thiele, & Hinz,
83 2016). In addition, some research studies have extracted building information by
84 integrating different sources of satellite images to fully exploit the advantages of
85 different data. For example, Xu et al. (2017a) extracted building information from a
86 high-density urban area using both high-resolution stereo and SAR data. Wegner,
87 Ziehn, and Soergel (2010) used both optical imagery and InSAR data to detect 3D
88 building information. Gamba and Houshmand (2002) used SAR and LiDAR data with
89 optical imagery to detect land cover types, a DTM and the 3D shapes of buildings.

90 Moreover, an increasing number of methods for the detection of building information
91 are based on high-resolution digital surface models (DSMs) generated from satellite
92 images (Lafarge, Descombes, Zerubia, & Pierrot-Deseilligny, 2010; Merciol &
93 Lefèvre, 2015; Davydova, Cui, & Reinartz, 2016). However, the accuracy and the
94 universality of the applicability of satellite image-based methods have been limited by
95 the cost or accessibility of high-spatial-resolution remotely sensed data (Weidner &
96 Förstner, 1995). Moreover, the interpretation of satellite (e.g., SAR and LiDAR)
97 images is also complicated.

98 Nevertheless, recent developments in location-based services and digital map services
99 have facilitated various applications for the extraction of urban morphological
100 information. Several open map services, including OpenStreetMap (OSM), ArcGIS
101 Online, Google Maps, Yahoo! Maps, and TIGER/Line Map, have been applied to
102 extract urban information (Chiang, Knoblock, Shahabi, & Chen, 2009; Malarvizhi et
103 al., 2016; Huber & Rus, 2016; Kaiser et al., 2017). While OSM has been applied for
104 some urban studies (Audebert, Le Saux, & Lefèvre, 2017; Lopes, Fonte, See, &
105 Bechtel, 2017), the function and architectural details of the buildings extracted
106 through OSM still need to be improved (Fan, Zipf, Fu, & Neis, 2014; Hecht, Kunze,
107 & Hahmann, 2013). Google has developed a series of application programming
108 interfaces (APIs) that allow users to extract useful urban information from Google
109 Maps. For example, many researchers have extracted urban canopy geometries from
110 street-view panoramas using the Google Street View (GSV) API. Openness and
111 greenery along a street can be mapped by calculating the sky view factor (SVF) and

112 green view index using GSV panoramas (Carrasco-Hernandez, Smedley, & Webb,
113 2015; Gong et al., 2018; Li, Ratti, & Seiferling, 2017; Yin & Wang, 2016; Zeng, Lu,
114 Li, & Li, 2018). Although GSV images are free and their developed results show high
115 accuracy, they have a well-known limitation in their spatial coverage and
116 accessibility. Moreover, GSV images are available and applicable only for mapping
117 the streetscapes of urban canyons in cities throughout the world and along major
118 routes where the Google car can travel. For other cities or other urban areas where the
119 Google car is not allowed, it is impossible to obtain any comprehensive
120 morphological information from GSV images.

121 The new trend in the extraction of 3D urban morphology consists of the combination
122 of satellite images with open map services (Haala & Anders, 1996; Suveg &
123 Vosselman, 2004; Over, Schilling, Neubauer, & Zipf, 2010). By combining satellite
124 images with open map services, the specific advantages of both satellite images (i.e., a
125 high accuracy and a large information content) and maps (i.e., a relatively simple
126 interpretation and open access availability) can be exploited. Therefore, the aims of
127 this study are (1) to develop a method for the acquisition of 3D urban morphology
128 information by integrating Google Maps with a freely available DSM that can be
129 easily applied to cities worldwide; (2) to generate 3D urban morphologies and
130 calculate urban morphological parameters in Hong Kong, a city with a complex urban
131 form; (3) to validate the urban morphology information pertaining to various urban
132 landscapes; and (4) to further discuss the limitations and advantages of this method, as
133 well as its applications. The proposed method will contribute to the scholarly

134 understanding and extraction of urban morphology in a highly efficient way using a
135 simple workflow. This approach can be applied to cities worldwide, especially those
136 that lack urban data. In practice, the results provide not only access to a freely open
137 urban dataset for researchers, town planners and architects but also new insights into
138 applications such as urban studies and urban planning related to or based on urban
139 morphology.

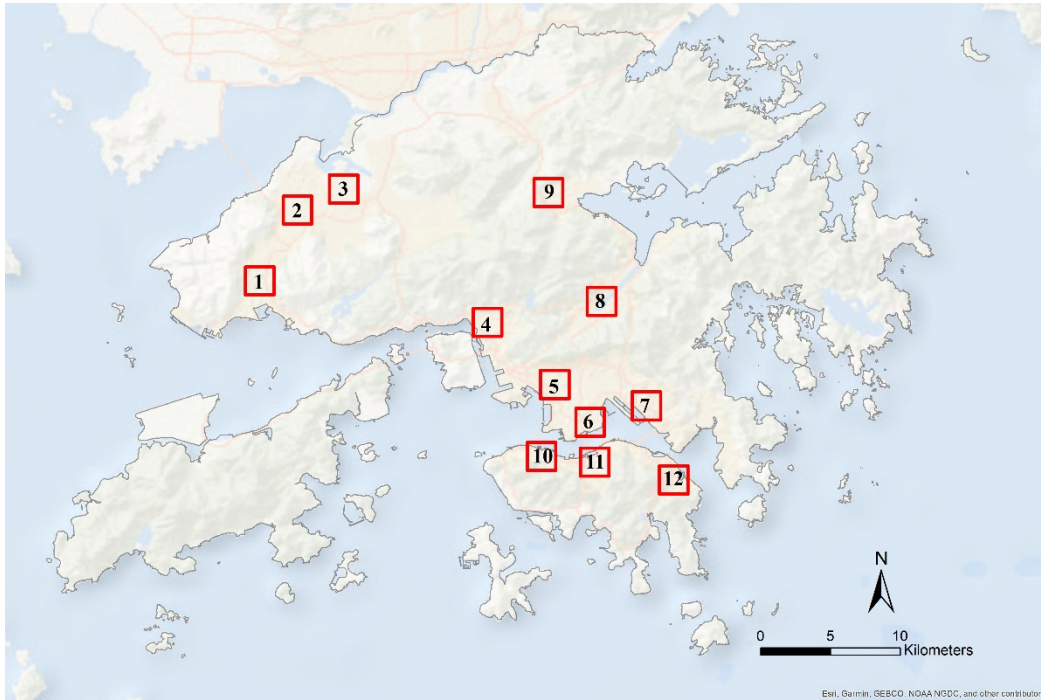
140 **2 MATERIALS AND METHODS**

141 **2.1 Study Area and Sample Sites**

142 In this study, Hong Kong — a large city with a complex urban morphology and a
143 unique geographical context — is selected as the testbed. Hong Kong is one of the
144 world’s most compact cities, with a population of over 7.3 million in a land area of
145 1,100 km². This extremely high population density shapes the unique urban form of
146 Hong Kong’s metro area. The high-density areas of Hong Kong are almost entirely
147 composed of densely packed high-rise buildings with podiums and deep street
148 canyons (Li et al., 2012). As a consequence of this high density, Hong Kong is facing
149 undesirable externalities such as thermal comfort issues, overcrowding, urban heat
150 island effects, poor air ventilation, and high air pollution concentrations in deep street
151 canyons. To improve the urban climate and environment, the strategic study entitled
152 “Hong Kong 2030+: Towards a Planning Vision and Strategy Transcending 2030”
153 (Planning Department of Hong Kong, 2016) has defined the future key strategic
154 planning direction as “Planning for a Livable High-density City”, which includes the

155 sensitive disposition of urban blocks, building setbacks, and the creation of a
156 breezeway/urban wind corridor, among other components.

157 For this study, a total of 12 rectangular areas (2 km x 2 km) with varied urban
158 landscapes have been sampled for the extraction of 3D urban morphology information
159 to provide a fair representation of Hong Kong's urban form, as shown in Figure 1. Six
160 sample sites are located in metropolitan areas (sites 5, 6, 7, 10, 11, and 12); four sites
161 are located in the new town areas (sites 1, 4, 8, and 9); and two sites are chosen from
162 industrial and rural areas (sites 2 and 3). The metropolitan sample areas are highly
163 urbanized and contain a number of extremely tall skyscrapers over 200 meters; the
164 dominant building type is very tall and sharp-edged buildings (Renganathan, 2005).
165 The sample sites located in the new town areas have more open spaces and street
166 canyons with a relatively low height-width ratio. According to a local climate zone
167 mapping of Hong Kong conducted by Wang, Ren, Xu, Lau, and Shi (2018), the main
168 type of built-up structure in the Kowloon district (metropolitan area) is the compact
169 high-rise, and the main type of built-up structure in the Yuen Long district (new town
170 area) is sparse construction. The podium-tower structure is the most generic planning
171 model and can be commonly found throughout Hong Kong (E Ng et al., 2005).



172

173 **Figure 1.** The locations of the 12 sample sites (2 km x 2 km) in Hong Kong.

174 **2.2 Data Source**

175 **2.2.1 Maps Static API**

176 Google Maps is an Internet open map service application and technology provided by
 177 Google that contains an urban morphology database for global cities. Google
 178 encourages the diverse usage of its products according to the Google Permissions of
 179 Using Google Maps, Google Earth and Street View (Google, 2015). Google launched
 180 the Google Maps API in June 2005 to allow developers to integrate Google Maps into
 181 their websites. The Maps Static API provided by Google Maps creates maps based on
 182 URL parameters sent through a standard HTTP request and returns the maps as an
 183 image (Google, 2018). The basic parameters that define a map include the “center
 184 coordinates”, a “zoom” level and the “size” of the map image (in pixels). Optionally,

185 by using the Maps Static API, users can employ the “style” parameter, which defines
186 a custom style to alter the presentation of specific features (roads, parks, built-up
187 areas, and building footprints) within the map; this parameter takes “feature” and
188 “element” arguments, identifying the abovementioned features based on a user-
189 defined style and a set of style operations to apply the selected features, making the
190 map a styled map. Therefore, building footprint information can be retrieved from
191 styled maps using the Maps Static API.

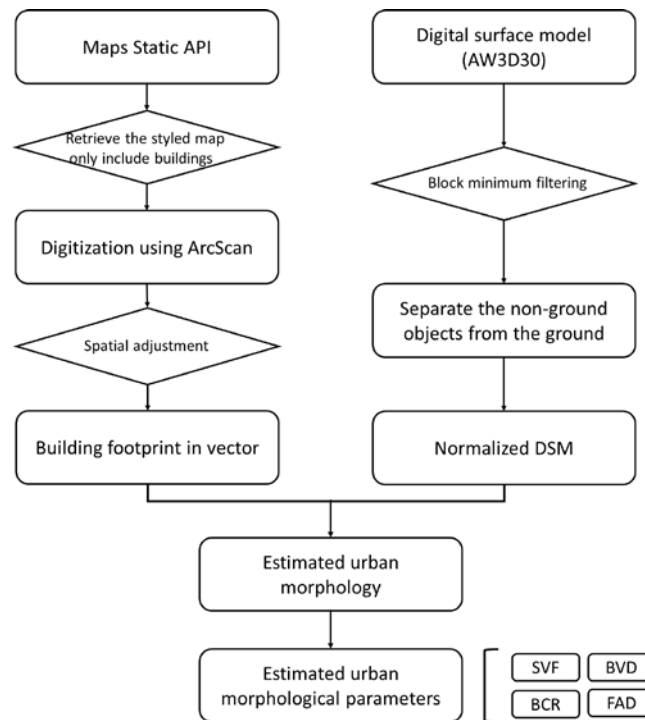
192 **2.2.2 Digital Surface Model Data**

193 There are two main categories of globally available digital elevation models (DEMs):
194 commercial DEMs and freely available DEMs. The Shuttle Radar Topography
195 Mission (SRTM), the Advanced Spaceborne Thermal Emission and Reflection
196 Radiometer Global DEM (ASTER GDEM), and the Advanced Land Observing
197 Satellite (ALOS) World 3D – 30 m (AW3D30) DSM are the three global-scale DEM
198 datasets that are currently available to the general public free of charge. All of these
199 DEM datasets provide a moderate resolution of approx. 30 meters (1 arcsec) and
200 capture almost the entire Earth’s surface. According to previous studies (Grohmann,
201 2018; Santillan & Makinano-Santillan, 2016), the AW3D30 DSM was found to be the
202 most accurate DEM dataset with the lowest mean error and root mean square error
203 (RMSE) compared to other freely available DEMs. Additionally, AW3D30 is the
204 newest global DEM dataset currently available; it was created based on the original
205 images from 2006 to 2011 acquired by the 5-meter mesh ALOS dataset, which is

206 considered to be the most precise global elevation dataset at present (Tadono et al.,
207 2014). Therefore, in this study, the AW3D30 dataset was selected for extracting
208 building height information. The AW3D30 dataset, which was released in 2015 by the
209 Japan Aerospace Exploration Agency, can be publicly obtained from
210 <http://www.eorc.jaxa.jp/ALOS/en/aw3d30/>. The AW3D30 tiles were downloaded and
211 saved in GeoTIFF format for further calculations using ArcMap 10.6 software.

212 **2.3 3D Urban Morphology Extraction**

213 The process of extracting urban morphology information includes two major steps: 1)
214 building footprint extraction and 2) building height extraction (Figure 2). The building
215 footprint extraction process was based on the styled maps obtained from the Maps
216 Static API, while the building heights were generated from the AW3D30 DSM. After
217 extracting the building heights and building footprints, the estimated urban
218 morphology within the study area was acquired. Thereafter, urban morphological
219 parameters, including the SVF, building coverage ratio (BCR), building volume
220 density (BVD), and frontal area density (FAD), were calculated based on the retrieved
221 building footprints and building heights.



222

223 **Figure 2.** A chart of the workflow for the 3D urban morphology extraction process
 224 proposed in this study.

225 2.3.1 Building Footprint Extraction

226 The presentation of standard Google Maps can be customized by applying customized
 227 styles using the Maps Static API. Therefore, styled maps can display features such as
 228 roads, parks, built-up areas, and other points of interest. The particular styles can be
 229 highlighted by defining the color or style by complementing the surrounding content
 230 on the page or even hiding features completely using the API. A Maps Static API
 231 URL must be of the following form:

232 [https://maps.googleapis.com/maps/api/staticmap?parameters.](https://maps.googleapis.com/maps/api/staticmap?parameters)

233 The parameters in the URL include location, map, feature and element parameters.

234 The location parameters determine the center coordinates of the map and the zoom

235 level. The map parameters define the characters of the map, such as its size and
236 format. The feature and element parameters determine the style of the map. The
237 feature parameters indicate the presence of elements on the map, such as roads, parks,
238 or other points of interest; for example, the syntax “feature:road” specifies the
239 selection of roads on the map. Elements, such geometries and labels, are
240 characteristics of features.

241 To display the building footprint information, styled maps within the study area were
242 created using the Maps Static API. The location of each map was defined in the study
243 area, and the zoom level was set to 17 to display the building footprints by setting the
244 location parameters. The images were formatted as png32, which provides a lossless
245 compression of the map. The features of the building footprints were selected by
246 defining the feature parameters, and the buildings were given black outlines using the
247 element parameters. Other features, such as roads and water, were turned off, and the
248 background was set to white to emphasize the building footprints in each map. An
249 example of a URL employed to retrieve a styled map has been included in the
250 supplementary materials. The building footprints retrieved by the URLs are displayed
251 in Figure 3.



252

253 **Figure 3.** Building footprints from the Maps Static API (map center: 22.33, 114.16,
254 zoom=17).

255 The maps were saved to local hard drives. The imagery was digitized in ArcScan
256 using ArcGIS to convert the building footprints into a vector format. ArcScan
257 provides tools to convert raster images into vector-based feature layers in a rapid and
258 automatic way. After digitization, a spatial adjustment was performed to assign the
259 coordinate system to the Hong Kong 1980 grid system for the retrieved vector based
260 on actual GIS data from the planning department of Hong Kong. The details of the
261 extracted building footprints within the study area are displayed in Figure 4 and
262 Figure S1 (in the supplementary materials).



263

264 **Figure 4.** Extraction of building footprints for site 5, shown above as an example. For
 265 all the other sites, please see Figure S1 in the supplementary materials.

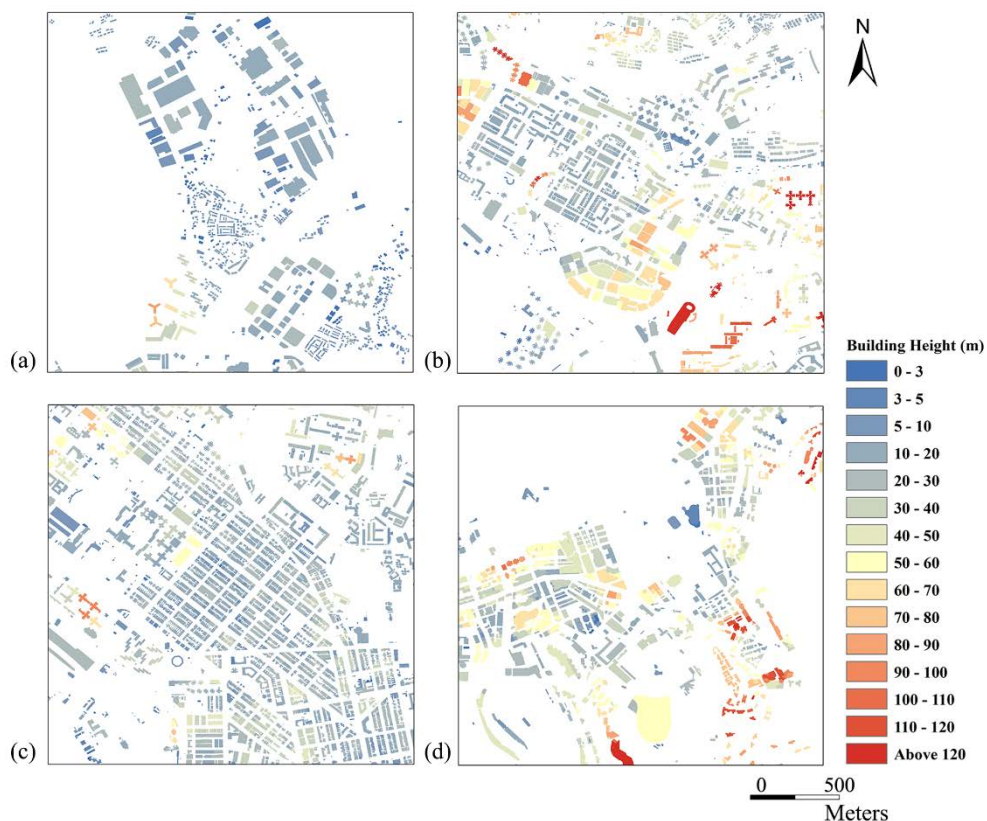
266 **2.3.2 Building Height Extraction**

267 The building height (BH) is an important urban morphological parameter that is
 268 widely used in weather forecasting models and urban canopy models. In this study,
 269 AW3D30 DSM images were used to extract building height information. The whole
 270 processing workflow for extracting the building height consists of two stages. The
 271 first stage is the generation of an nDSM. A DSM is a representation of the Earth's
 272 surface that contains all objects higher than the ground, e.g., trees and buildings. To
 273 extract buildings, an approximation of the bare earth (a continuous ground terrain,
 274 known as a digital elevation model, DEM) was determined first to separate the
 275 nonground objects from the ground. The difference between the original DSM and the

276 approximated DEM is named the normalized DSM (nDSM), which contains the
277 height information of all nonground objects (Equation 1).

$$nDSM = DSM - DEM \quad \text{Equation 1}$$

278 For this study, the block minimum filtering method (Wack & Wimmer, 2002) was
279 adopted to generate the DEM by taking the minimum elevation within a certain area.
280 Considering the resolution of the raw DSM images, the block minimum filter was
281 applied with a grid size of 300 meters. The second stage of building height extraction
282 is to separate buildings from other objects by assigning the nDSM to each building
283 footprint using the building information acquired from the Maps Static API. In this
284 study, BH refers to the average building height of an individual building. The
285 estimated building heights within the sites of the study area are displayed in Figure 5.



286

287 **Figure 5.** The estimated building heights in (a) Site 3, (b) Site 4, (c) Site 5, and (d)
288 Site 11.

289 **2.3.3 Derivation of Urban Morphological Parameters**

290 The building coverage ratio (BCR) is the ratio of the building area to the total land lot
291 size. The BCR has a strong influence on the local thermal environment (Zhan, Meng,
292 & Xiao, 2015) and has an impact on local wind velocity ratios (Kubota, Miura,
293 Tominaga, & Mochida, 2008; Edward Ng et al., 2011). The results show that the
294 higher the gross BCR is, the lower the observable wind velocity ratio will be. The
295 BCR is calculated as follows:

$$296 \quad \text{BCR} = \frac{\sum_{i=1}^N C_i}{S_L}$$

297 *Equation 2*

298 where C_i is the area of building i on the plan area and S_L is the size of the plan area.

299 The building volume density (BVD) represents the building density over the land lot
300 size. The BVD also influences the local thermal environment (Chen et al., 2012). The
301 BVD is calculated as the total volume of buildings divided by the land lot size:

$$302 \quad \text{BVD} = \frac{\sum_{i=1}^N (C_i \times h_i)}{S_L} \quad \text{Equation 3}$$

303 where C_i is the area of building i on the land lot, h_i is the height of building i and
304 S_L is the size of the plan area.

305 The sky view factor is defined as “the ratio of the amount of the sky ‘seen’ from a
306 given point on a surface to that potentially available (i.e., the proportion of the sky

307 hemisphere subtended by a horizontal surface)” (Oke, 1987, 404). The SVF can be
 308 used to quantify the ratio of the diffuse irradiance at a given point to that of an
 309 unobstructed horizontal surface. The SVF ranges between one (no influence of the
 310 adjacent terrain) and zero (no sky view and maximal influence of the adjacent terrain).
 311 The SVF is an important indicator for urban heat islands (Chen et al., 2012; Gál,
 312 Lindberg, & Unger, 2009; Scarano & Mancini, 2017). The SVF can be calculated
 313 based on DSM data by adding building heights to a DEM at a very fine scale (Dozier
 314 & Frew, 1990). In this study, the DSM newly generated from the retrieved building
 315 heights and the DEM with a 2-m resolution were used to calculate the SVF with the
 316 following expression derived from previous work (Böhner & Antonić, 2009; Scarano
 317 & Sobrino, 2015):

$$318 \quad SVF = \frac{1}{2\pi} \int_0^{2\pi} [\cos \beta \cos^2 \varphi + \sin \beta \cos(\phi - \alpha)(90 - \varphi - \sin \varphi \cos \varphi)] d\phi$$

319 *Equation 4*

320 where β and α are the surface slope angle and surface aspect, respectively, calculated
 321 from the DSM, φ is the horizon angle and ϕ is the azimuth direction.

322 The frontal area density (FAD) refers to a building’s frontal areas that face the wind
 323 over a site’s area. The FAD is an important parameter for describing the surface
 324 roughness and for detecting the air paths in urban areas, which can provide a basic
 325 understanding of urban ventilation at the pedestrian level. Ng et al. (2011) conducted
 326 a study on detecting the wind environment in the Kowloon Peninsula of Hong Kong
 327 based on the FAD and found that the wind velocity ratio is more dependent on the

328 urban morphology characteristics at the podium layer (0-15 m) than at the canopy
 329 layer (0-60 m); a 10% increase in the FAD can result in a 2.5% decrease in the wind
 330 velocity ratio at the podium layer. The FAD in one wind direction is calculated as:

$$FAD(\theta) = \frac{\sum_i A_F(\theta)}{S}$$

332 *Equation 5*

333 where $A_F(\theta)$ represents the frontal area of building i in the wind direction θ and S
 334 represents the size of the uniform grid, which is chosen as 100 m, 250 m and 500 m in
 335 this study.

336 **2.4 Validation of the Results**

337 To assess the accuracy of the extracted urban morphology, the estimated urban
 338 morphological parameters were compared with the actual parameters at resolutions of
 339 100 m, 250 m and 500 m. First, a linear regression model was established between the
 340 estimated and actual urban morphological parameters. The R-squared value was used
 341 to assess the quality of the estimated results, where a higher R-squared value indicates
 342 a better prediction result. The calculation of R is displayed in the following equation:

$$R = \frac{n \sum_{i=1}^n x_i y_i - (\sum_{i=1}^n x_i)(\sum_{i=1}^n y_i)}{\sqrt{(n \sum_{i=1}^n x_i^2) - (\sum_{i=1}^n x_i)^2} \times \sqrt{(n \sum_{i=1}^n y_i^2) - (\sum_{i=1}^n y_i)^2}} \quad \text{Equation 6}$$

344 where n is the total number of observations, y is the estimated morphological
 345 parameter, and x is the actual morphological parameter. Second, the root mean square
 346 error (RMSE) was calculated to examine the errors of the predicted results. The
 347 RMSE is a quadratic scoring rule that also measures the average magnitude of the

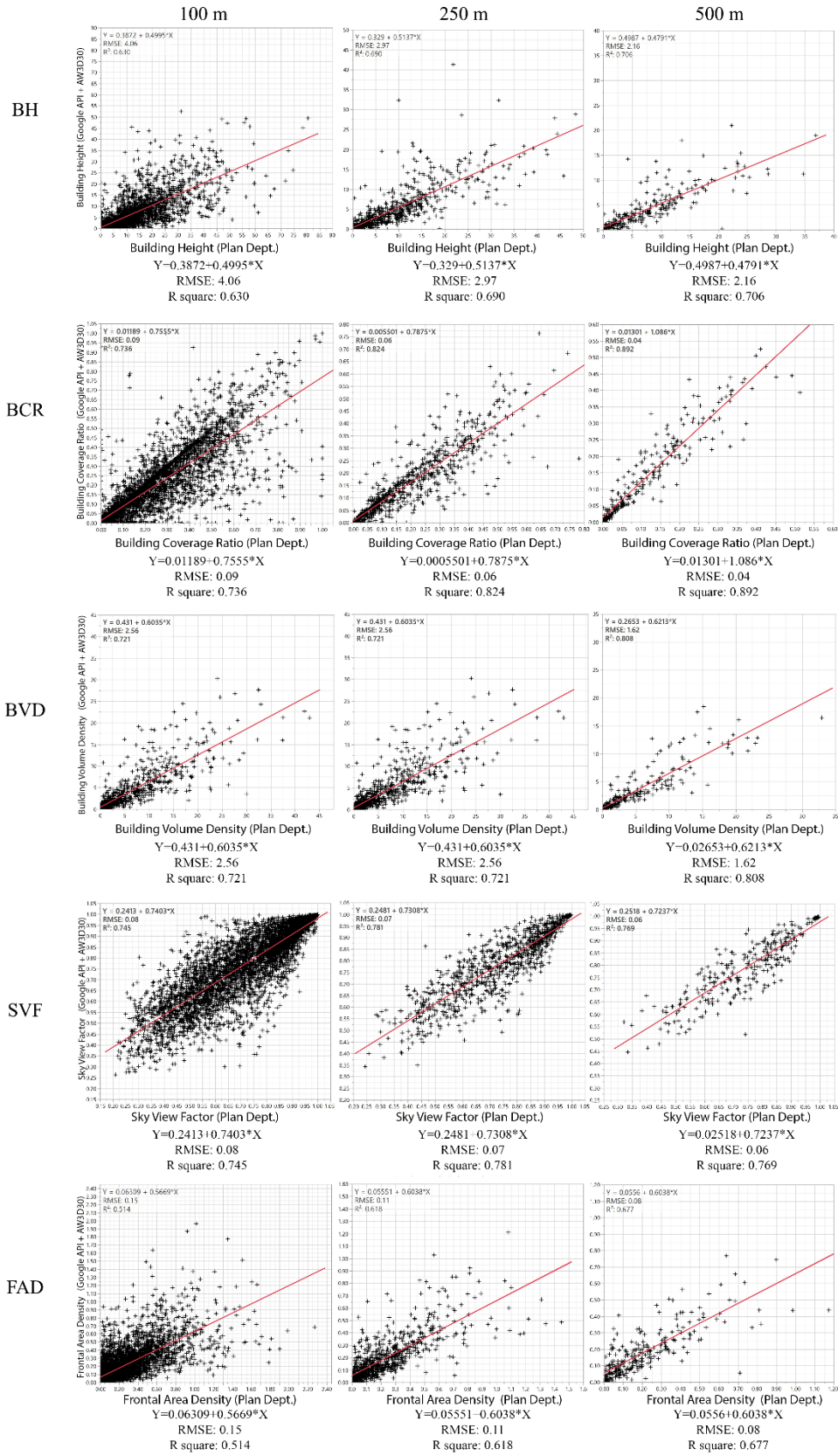
348 error; it is the square root of the average of the squared differences between the
349 predicted values and the actual observations. The lower the RMSE is, the better the
350 estimates are.

351 $RMSE =$

352 $\sqrt{\frac{1}{n} \sum_{i=1}^n (y_i - x_i)^2}$ *Equation 7*

353 **3 RESULTS**

354 Based on the retrieved urban morphology information, a set of urban morphological
355 parameters was further calculated and aggregated at resolutions of 100 m, 250 m and
356 500 m to test the accuracy and possible applications of the results at different scales.
357 Figure 6 shows the actual and estimated urban morphological parameters at grid
358 resolutions of 100 m, 250 m and 500 m.



360 **Figure 6.** *The actual and estimated urban morphological parameters at grid*
361 *resolutions of 100 m, 250 m and 500 m.*

362 **4 DISCUSSION**

363 **4.1 Analyzing the Results of Extracting Building Morphological Parameters**

364 **4.1.1 Building Coverage Ratio**

365 The validation of the results based on the 100 m grid shows good consistency between
366 the actual and estimated BCR values with an $R^2 = 0.736$ and an RMSE of less than
367 9%. As shown in the regression plot of the BCR at a 100 m grid size, a slight but
368 systematic underestimation can be clearly observed. This underestimation not only
369 appears at specific intervals but can be seen along almost the entire range of the data.
370 With an increase in the grid size, the level of underestimation decreases. The
371 relationship between the actual and estimated BCR values further increases to $R^2 =$
372 0.824 at a grid size of 250 m and $R^2 = 0.892$ at a grid size of 500 m. These results
373 indicate that the estimated BCR using the method proposed herein can fulfill the
374 requirements of input data for meteorological research and weather forecasting
375 models, such as the Weather Research and Forecasting (WRF) model. Moreover, the
376 estimation results at 250 m could be adopted for research at a fine spatial scale
377 because these results already provide a reasonably accurate depiction of single urban
378 neighborhoods and small street blocks, potentially providing a valuable input dataset
379 for reducing the spatial uncertainties in environmental health risk assessments.

4.1.2 Building Height

380
381 The estimation of the building height has a reasonable relationship with R^2 values of
382 0.630, 0.690, and 0.706 at grid sizes of 100 m, 250 m and 500 m, respectively. Similar
383 to the estimation of the BCR, a general slight underestimation is observed. In contrast
384 to the BCR estimation, however, the estimation performance of the BH does not
385 increase considerably as the grid size increases. For example, the performance
386 increases only slightly, by approximately 11%, when the grid size is enlarged by a
387 factor of five. Moreover, the regression analysis also indicates that the regression
388 relationship between the actual and estimated BH values varies among different urban
389 forms. As indicated in the regression plot of the BH at a grid size of 100 m, the Hung
390 Hom site in the Kowloon Peninsula has a significant difference (the different
391 relationship is shown as the separately plotted red regression line). Moreover, the
392 estimation results for areas with generally low building heights are unsatisfying,
393 which may limit the application of the proposed method in urban forms with a low-
394 rise building environment. As indicated by these findings from the BH estimation,
395 nonlinear fitting models are needed for further investigation and might need to be
396 incorporated into the algorithm for improving the proposed method.

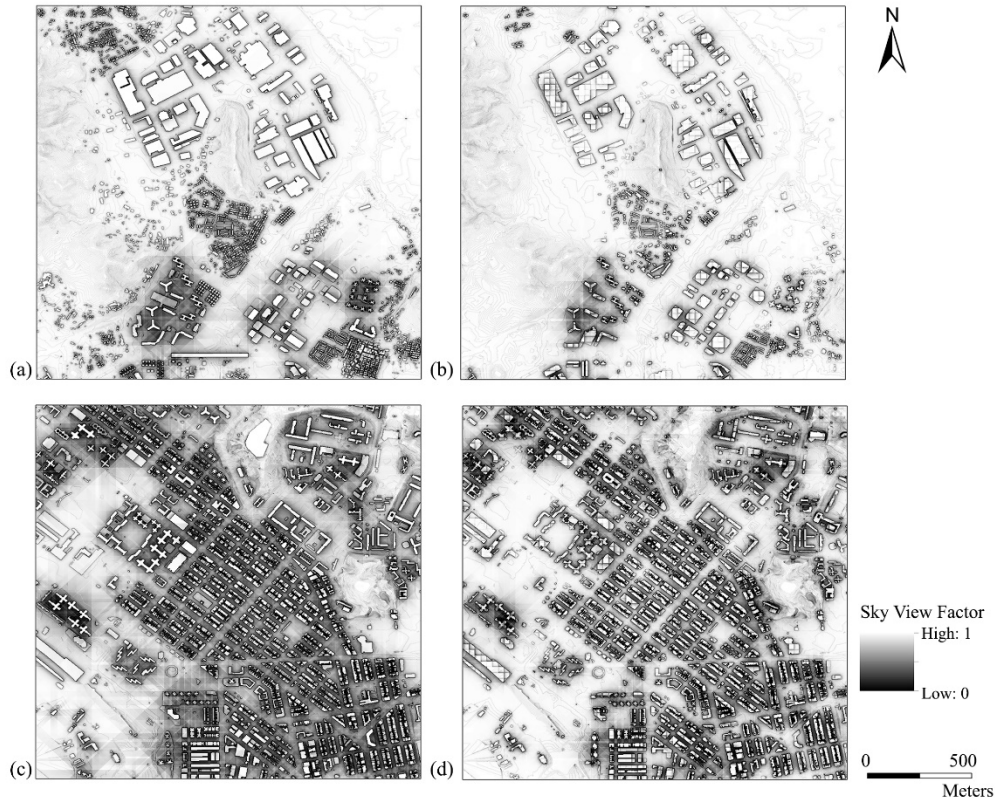
4.1.3 Building Volume Density

397
398 A slight overall underestimation was also observed in the estimation of the BVD at all
399 grid sizes. This might be a result of the observed underestimation in both the BCR and
400 the BH. However, there are no particular patterns among the different quantiles of the

401 BVD. The outliers are mostly randomly distributed along both sides of the regression
402 line. Similar to the BCR estimation results, there is consistency between the actual
403 and estimated values since the R^2 values increase from 0.599 to 0.808 as the grid size
404 increases. The proposed method provides a usable estimation of the BVD at a 500 m
405 spatial resolution, which is potentially applicable as an input to regional
406 meteorological and weather forecasting models. However, the overall underestimation
407 mentioned above will need to be calibrated based on site survey data.

408 **4.1.4 Sky View Factor**

409 For the relationship between the SVF calculated based on actual building data and
410 that based on estimated building data, the R^2 ranges from 0.745 to 0.781 for the three
411 different grid sizes. Similar to the BH, the estimation performance of the SVF does
412 not increase considerably as the grid size increases. The overall estimation
413 performance of the SVF remains stable across different grid sizes and is therefore not
414 sensitive to the resolution. No obvious underestimation or overestimation was
415 identified. The above findings indicate that the building data generated by using the
416 Google Maps API and the AW3D30 dataset provide a reasonably good estimation of
417 the SVF (Figure 7). Considering that the results remain stable at varying spatial
418 resolutions (ranging from 100 m to 500 m), the SVF estimation results are applicable
419 to the investigation of city-scale outdoor thermal comfort; the estimated SVF could
420 also be used as a reference for the spatial investigation of city-scale urban climate and
421 city energy exchanges.



422

423 **Figure 7.** (a) The actual sky view factor of Site 3. (b) The estimated sky view factor
 424 of Site 3. (c) The actual sky view factor of Site 5. (d) The estimated sky view factor of
 425 Site 5.

426 **4.1.5 Frontal Area Density**

427 Similar to the BVD, a slight overall underestimation was observed in the estimation of
 428 the FAD at all different grid sizes, which might be due to the observed
 429 underestimation in both the BCR and the BH. However, there are no particular
 430 patterns among the different quantiles of the FAD. The data points are mostly
 431 randomly distributed along both sides of the regression line. Different from the BH
 432 estimation results, the regression analysis of the estimated FAD indicates that the
 433 regression relationship between the actual and estimated BH values does not vary

434 among different urban forms. Moreover, the estimation performance of the FAD
435 slightly increases as the grid size increases. The R^2 values reach 0.514 and 0.618 at
436 grid sizes of 100 m and 250 m, respectively, and a usable estimation performance of
437 $R^2 = 0.677$ is achieved at a grid size of 500 m. These validation results indicate that
438 the FAD estimation results acquired at a spatial resolution of 500 m by using the
439 method proposed in the present study have the potential to be further calibrated with a
440 site survey and subsequently adopted as input data for meteorological research and
441 weather forecasting models, such as the WRF model. By investigating the geolocation
442 of the outliers in the regression, it can be found that a low actual FAD in reality but a
443 high estimated FAD in the extracted building dataset is due to an overestimation
444 corresponding to the low-rise, sparsely built village clusters on the hillslope. To
445 resolve this issue, the method of handling the AW3D30 dataset should be fine-tuned
446 to correct for the estimated building heights of low-rise buildings on slopes or at
447 relatively high elevations. A high actual FAD in reality corresponding to a low
448 estimated FAD in the extracted building dataset is also observed, which is due to the
449 underestimation caused by unidentified skyscraper towers atop the large building
450 podiums in the footprint data extracted using the Google Maps API. These
451 under/overestimations are not considered to be critical issues since the above
452 situations are due to unique urban morphological characteristics, which do not occur
453 frequently in most cities.

4.2 Limitations and Future Research

454
455 As shown in the validation of these results, although the newly developed 3D urban
456 morphology extraction method performs reasonably well in estimating most urban
457 morphological parameters in the majority of urban forms, slight overestimations or
458 underestimations have been observed in the test results when applying this method in
459 Hong Kong. By identifying the geolocations of the overestimated or underestimated
460 areas, it has been found that many of these cases are due to the highly complex urban
461 form of Hong Kong, which should not be as critical an issue in other cities throughout
462 the world. More specifically, the elevation information within the AW3D30 dataset
463 over Hong Kong tends to have a lower accuracy than the information over other
464 cities, as it is more challenging to extract building heights from the extremely high-
465 density and unique urban physical environment of Hong Kong (Xu et al., 2017b). All
466 the above findings indicate that future research should focus on fine-tuning the
467 method for handling the AW3D30 dataset to further improve the estimation of the
468 building heights in some particular scenarios (i.e., involving low-rise buildings on
469 sloped land or at relatively high elevations or involving skyscraper towers combined
470 with large building podiums). Future research should also focus on testing the
471 proposed method in other cities with varying urban morphological characteristics.

472 To further improve the robustness of the results in different urban scenarios all over
473 the world, we would like to recommend that the potential users of this method
474 conduct on-site building surveys in their own cities (or acquire building survey data
475 from local authorities) based on a partial sampling scheme. These building survey

476 data could be used as the ground truth for calibrating and fine-tuning the results for
477 their particular urban forms.

478 Roofs are another important component of urban morphology in an urban
479 environment. The geometry of a roof can be detected using the Maps Static API.
480 However, variations in the roof height cannot be fully represented due to the coarse
481 spatial resolution of the AW3D30 dataset. Thus, this study focused only on the
482 footprints and heights of buildings.

483 **5 CONCLUSIONS**

484 This study developed an easy and highly efficient method for extracting 3D urban
485 morphology information by using open-source data. Our newly developed method
486 provides researchers with a possible way to collect 3D urban and building
487 morphology information since all raw data are freely available and accessible to the
488 public. The developed method consists of a two-step procedure: building footprints
489 are extracted from styled maps using the Maps Static API, and building heights are
490 extracted from open-source DSM data, i.e., the AW3D30 dataset. The proposed
491 method was applied in Hong Kong, a city with a varying and complex urban
492 morphology. The 3D urban morphology in Hong Kong was extracted using the
493 developed approach, and the urban morphological parameters, including the building
494 height, building coverage ratio, building volume density, sky view factor and frontal
495 area density, were calculated. As the proposed approach is generic and uses open-
496 source data, given the reliability of the results, this study demonstrates that the

497 developed method could be adopted and applied to any other city or region on Earth.
498 The urban morphological parameters estimated based on the newly compiled 3D
499 urban morphology data were validated by a comparison with the actual parameters in
500 different urban landscapes at various resolutions of 100 m, 250 m and 500 m to
501 explore the potential usage of the developed methodology. The results show a
502 reasonably good and useable accuracy and a wide applicability of the newly proposed
503 method. In particular, a higher accuracy was identified in areas with a less complex
504 urban form, and the accuracy increased with the spatial resolution of the urban
505 morphological parameters. The high accuracy of the urban morphological parameters
506 extracted based on the grid with a 500 m spatial resolution indicates that the 3D urban
507 morphological information detected using the proposed method is readily applicable
508 to serve as input data for mesoscale climate and environment modeling simulations,
509 such as WRF simulations. The presented method and the retrieved variables can also
510 be used as environmental variables in environmental exposure investigations, public
511 health risk assessments, and urban carbon emissions mapping. Therefore, this 3D
512 urban morphology extraction method can contribute to sustainable urban development
513 in general and practical applications in the implementation of town planning exercises
514 and urban development decision-making.

515 **ACKNOWLEDGMENTS**

516 This research is supported by the General Research Fund (GRF Project Number:
517 14611015, 14643816) from the Research Grants Council (RGC) of Hong Kong. Part

518 of the research was developed during the Young Scientists Summer Program at the
519 International Institute for Applied Systems Analysis, Laxenburg (Austria) with
520 financial support from the Ecosystems Services and Management program. The
521 authors appreciate reviewers for their insightful comments and constructive
522 suggestions on our research work. The authors also want to thank editors for their
523 patient and meticulous work for our manuscript.

524 **REFERENCE**

- 525 Audebert, N., Le Saux, B., & Lefèvre, S. (2017). *Joint learning from earth observation and*
526 *openstreetmap data to get faster better semantic maps*. Paper presented at the
527 EARTHVISION 2017 IEEE/ISPRS CVPR Workshop. Large Scale Computer Vision
528 for Remote Sensing Imagery.
- 529 Böhner, J., & Antonić, O. (2009). Land-surface parameters specific to topo-climatology.
530 *Developments in Soil Science*, 33, 195-226. DOI: 10.1016/S0166-2481(08)00008-1
- 531 Burkhart, G., Bergen, Z., Carande, R., Hensley, W., Bickel, D., & Fellerhoff, J. (1996).
532 *Elevation correction and building extraction from interferometric SAR imagery*.
533 Paper presented at the Geoscience and Remote Sensing Symposium, 1996.
534 IGARSS'96.'Remote Sensing for a Sustainable Future.', International. DOI:
535 10.1109/IGARSS.1996.516434
- 536 Carrasco-Hernandez, R., Smedley, A. R., & Webb, A. R. (2015). Using urban canyon
537 geometries obtained from Google Street View for atmospheric studies: Potential
538 applications in the calculation of street level total shortwave irradiances. *Energy and*
539 *Buildings*, 86, 340-348. DOI: 10.1016/j.enbuild.2014.10.001
- 540 Chen, L., Ng, E., An, X., Ren, C., Lee, M., Wang, U., & He, Z. (2012). Sky view factor
541 analysis of street canyons and its implications for daytime intra-urban air temperature
542 differentials in high-rise, high-density urban areas of Hong Kong: a GIS-based
543 simulation approach. *International Journal of Climatology*, 32(1), 121-136. DOI:
544 10.1002/joc.2243
- 545 Chiang, Y.-Y., Knoblock, C. A., Shahabi, C., & Chen, C.-C. (2009). Automatic and accurate
546 extraction of road intersections from raster maps. *GeoInformatica*, 13(2), 121-157.
547 DOI: 10.1007/s10707-008-0046-3

- 548 Cionco, R. M., & Ellefsen, R. (1998). High resolution urban morphology data for urban wind
549 flow modeling. *Atmospheric Environment*, 32(1), 7-17. DOI: 10.1016/S1352-
550 2310(97)00274-4
- 551 Davydova, K., Cui, S., & Reinartz, P. (2016, October). Building footprint extraction from
552 digital surface models using neural networks. In *Image and Signal Processing for*
553 *Remote Sensing XXII* (Vol. 10004, p. 100040J). International Society for Optics and
554 Photonics. DOI: 10.5194/isprs-archives-XLII-1-W1-481-2017
- 555 Diamantini, C., & Zanon, B. (2000). Planning the urban sustainable development The case of
556 the plan for the province of Trento, Italy. *Environmental impact assessment*
557 *review*, 20(3), 299-310. DOI: 10.1016/S0195-9255(00)00042-1
- 558 Dozier, J., & Frew, J. (1990). Rapid calculation of terrain parameters for radiation modeling
559 from digital elevation data. *IEEE Transactions on Geoscience and Remote Sensing*,
560 28(5), 963-969. DOI: 10.1109/36.58986
- 561 Dubois, C., Thiele, A., & Hinz, S. (2016). Building detection and building parameter retrieval
562 in InSAR phase images. *ISPRS Journal of Photogrammetry and Remote*
563 *Sensing*, 114, 228-241. DOI: 10.1016/j.isprsjprs.2016.02.009
- 564 Fan, H., Zipf, A., Fu, Q., & Neis, P. (2014). Quality assessment for building footprints data
565 on OpenStreetMap. *International Journal of Geographical Information Science*,
566 28(4), 700-719. DOI: 10.1080/13658816.2013.867495
- 567 Gál, T., Lindberg, F., & Unger, J. (2009). Computing continuous sky view factors using 3D
568 urban raster and vector databases: comparison and application to urban climate.
569 *Theoretical and applied climatology*, 95(1-2), 111-123. DOI: 10.1007/s00704-007-
570 0362-9
- 571 Gamba, P., & Houshmand, B. (2002). Joint analysis of SAR, LIDAR and aerial imagery for
572 simultaneous extraction of land cover, DTM and 3D shape of buildings. *International*
573 *Journal of Remote Sensing*, 23(20), 4439-4450. DOI: 10.1080/01431160110114952
- 574 Gamba, P., Houshmand, B., & Sacconi, M. (2000). Detection and extraction of buildings from
575 interferometric SAR data. *IEEE Transactions on Geoscience and Remote Sensing*,
576 38(1), 611-617. DOI: 10.1109/36.823956
- 577 Gong, F.-Y., Zeng, Z.-C., Zhang, F., Li, X., Ng, E., & Norford, L. K. (2018). Mapping sky,
578 tree, and building view factors of street canyons in a high-density urban environment.
579 *Building and Environment*, 134, 155-167. DOI: 10.1016/j.buildenv.2018.02.042
- 580 Google. (2015). Permissions. Retrieved from
581 <https://www.google.com/permissions/geoguidelines/>
- 582 Google. (2018). Maps Static API. Retrieved from
583 <https://developers.google.com/maps/documentation/maps-static/dev-guide>

- 584 Grohmann, C. H. (2018). Evaluation of TanDEM-X DEMs on selected Brazilian sites:
585 Comparison with SRTM, ASTER GDEM and ALOS AW3D30. *Remote Sensing of*
586 *Environment*, 212, 121-133. DOI:10.1016/j.rse.2018.04.043
- 587 Haala, N., & Anders, K.-H. (1996). Fusion of 2D-GIS and image data for 3D building
588 reconstruction. *International Archives of Photogrammetry and Remote Sensing*, 31,
589 285-290.
- 590 Hao, L., Zhang, Y., & Cao, Z. (2016, July). Building extraction from stereo aerial images
591 based on multi-layer line grouping with height constraint. In *2016 IEEE International*
592 *Geoscience and Remote Sensing Symposium (IGARSS)* (pp. 445-448). IEEE. DOI:
593 10.1109/IGARSS.2016.7729110
- 594 He, W., Jäger, M., Reigber, A., & Hellwich, O. (2008). *Building extraction from polarimetric*
595 *SAR data using mean shift and conditional random fields*. Paper presented at the
596 Proc. 7th Eur. Conf. Synth. Aperture Radar (EUSAR).
- 597 Hecht, R., Kunze, C., & Hahmann, S. (2013). Measuring completeness of building footprints
598 in OpenStreetMap over space and time. *ISPRS International Journal of Geo-*
599 *Information*, 2(4), 1066-1091. DOI: 10.3390/ijgi2041066
- 600 Huber, S., & Rust, C. (2016). Calculate travel time and distance with OpenStreetMap data
601 using the Open Source Routing Machine (OSRM). *The Stata Journal*, 16(2), 416-423.
- 602 Johansson, E. (2006). Influence of urban geometry on outdoor thermal comfort in a hot dry
603 climate: A study in Fez, Morocco. *Building and Environment*, 41(10), 1326-1338.
604 DOI: 10.1016/j.buildenv.2005.05.022
- 605 Kaiser, P., Wegner, J. D., Lucchi, A., Jaggi, M., Hofmann, T., & Schindler, K. (2017).
606 Learning aerial image segmentation from online maps. *IEEE Transactions on*
607 *Geoscience and Remote Sensing*, 55(11), 6054-6068. DOI:
608 10.1109/TGRS.2017.2719738
- 609 Kubota, T., Miura, M., Tominaga, Y., & Mochida, A. (2008). Wind tunnel tests on the
610 relationship between building density and pedestrian-level wind velocity:
611 Development of guidelines for realizing acceptable wind environment in residential
612 neighborhoods. *Building and Environment*, 43(10), 1699-1708.
613 DOI:10.1016/j.buildenv.2007.10.015
- 614 Lafarge, F., Descombes, X., Zerubia, J., & Pierrot-Deseilligny, M. (2010). Structural
615 approach for building reconstruction from a single DSM. *IEEE Transactions on*
616 *Pattern Analysis and Machine Intelligence*, 32(1), 135-147. DOI:
617 10.1109/TPAMI.2008.281
- 618 Lau, K. K.-L., Chung, S. C., & Ren, C. (2019). Outdoor thermal comfort in different urban
619 settings of sub-tropical high-density cities: An approach of adopting local climate

- 620 zone (LCZ) classification. *Building and Environment*, 154, 227-238.
 621 DOI:10.1016/j.buildenv.2019.03.005
- 622 Li, T. T., Gao, Y. L., Wei, Z. H., Wang, J., Guo, Y. F., Liu, F., . . . Cheng, Y. L. (2012).
 623 Assessing Heat-related Mortality Risks in Beijing, China. *Biomedical and*
 624 *Environmental Sciences*, 25(4), 458-464. DOI:10.3967/0895-3988.2012.04.011
- 625 Li, X., Ratti, C., & Seiferling, I. (2017). *Mapping urban landscapes along streets using*
 626 *google street view*. Paper presented at the International Cartographic Conference.
- 627 Lopes, P., Fonte, C., See, L., & Bechtel, B. (2017). *Using OpenStreetMap data to assist in the*
 628 *creation of LCZ maps*. Paper presented at the Urban Remote Sensing Event (JURSE),
 629 2017 Joint. DOI: 10.1109/JURSE.2017.7924630
- 630 Luckman, A., & Grey, W. (2003). Urban building height variance from multibaseline ERS
 631 coherence. *IEEE Transactions on Geoscience and Remote Sensing*, 41(9), 2022-2025.
 632 DOI: 10.1109/TGRS.2003.815236
- 633 Malarvizhi, K., Kumar, S. V., & Porchelvan, P. (2016). Use of high resolution google earth
 634 satellite imagery in landuse map preparation for urban related applications. *Procedia*
 635 *Technology*, 24, 1835-1842. DOI: 10.1016/j.protcy.2016.05.231
- 636 Merciol, F., & Lefèvre, S. (2015, July). Fast building extraction by multiscale analysis of
 637 digital surface models. In *2015 IEEE International Geoscience and Remote Sensing*
 638 *Symposium (IGARSS)* (pp. 553-556). IEEE. DOI: 10.1109/IGARSS.2015.7325823
- 639 Ng, E., Tam, I., Ng, A., Givoni, B., Katzschner, L., Kwok, K., & Cheng, V. (2005).
 640 Feasibility study for establishment of air ventilation assessment system–final report.
 641 *Hong Kong: Department of Architecture, Chinese University of Hong Kong*, 16.
- 642 Ng, E., Yuan, C., Chen, L., Ren, C., & Fung, J. C. (2011). Improving the wind environment in
 643 high-density cities by understanding urban morphology and surface roughness: a
 644 study in Hong Kong. *Landscape and Urban Planning*, 101(1), 59-74. DOI:
 645 10.1016/j.landurbplan.2011.01.004
- 646 Nichol, J. E. (1996). High-resolution surface temperature patterns related to urban
 647 morphology in a tropical city: A satellite-based study. *Journal of applied*
 648 *meteorology*, 35(1), 135-146.
- 649 Nowak, D. J., Hirabayashi, S., Bodine, A., & Greenfield, E. (2014). Tree and forest effects on
 650 air quality and human health in the United States. *Environmental Pollution*, 193, 119-
 651 129. DOI: 10.1016/j.envpol.2014.05.028
- 652 Oke, T. R. (1987). *Boundary layer climates*: Routledge.
- 653 Over, M., Schilling, A., Neubauer, S., & Zipf, A. (2010). Generating web-based 3D City
 654 Models from OpenStreetMap: The current situation in Germany. *Computers*,

- 655 *Environment and urban systems*, 34(6), 496-507. DOI:
656 10.1016/j.compenvurbsys.2010.05.001
- 657 Paparoditis, N., Cord, M., Jordan, M., & Cocquerez, J.-P. (1998). Building detection and
658 reconstruction from mid-and high-resolution aerial imagery. *Computer vision and*
659 *image understanding*, 72(2), 122-142. DOI: 10.1006/cviu.1998.0722
- 660 Planning Department of Hong Kong. (2016). *Hong Kong 2030+ Planning and Urban Design*
661 *for a Liveable High-Density City*. Retrieved from
662 [http://www.hk2030plus.hk/document/Planning%20and%20Urban%20Design%20for](http://www.hk2030plus.hk/document/Planning%20and%20Urban%20Design%20for%20a%20Liveable%20High-Density%20City_Eng.pdf)
663 [%20a%20Liveable%20High-Density%20City_Eng.pdf](http://www.hk2030plus.hk/document/Planning%20and%20Urban%20Design%20for%20a%20Liveable%20High-Density%20City_Eng.pdf)
- 664 Renganathan, G. J. H. T. O. (2005). Urban design factors influencing outdoor temperature in
665 high-risehigh-density residential developments in the coastal zone of Hong Kong.
666 *HKU Theses Online (HKUTO)*.
- 667 Rottensteiner, F., & Briese, C. (2002). A new method for building extraction in urban areas
668 from high-resolution LIDAR data. *International Archives of Photogrammetry Remote*
669 *Sensing and Spatial Information Sciences*, 34(3/A), 295-301.
- 670 Santillan, J. R., & Makinano-Santillan, M. (2016). VERTICAL ACCURACY
671 ASSESSMENT OF 30-M RESOLUTION ALOS, ASTER, AND SRTM GLOBAL
672 DEMS OVER NORTHEASTERN MINDANAO, PHILIPPINES. *International*
673 *Archives of the Photogrammetry, Remote Sensing & Spatial Information Sciences*, 41,
674 149-156. DOI:10.5194/isprsarchives-XLI-B4-149-2016
- 675 Scarano, M., & Mancini, F. (2017). Assessing the relationship between sky view factor and
676 land surface temperature to the spatial resolution. *International Journal of Remote*
677 *Sensing*, 38(23), 6910-6929. DOI: 10.1080/01431161.2017.1368099
- 678 Scarano, M., & Sobrino, J. (2015). On the relationship between the sky view factor and the
679 land surface temperature derived by Landsat-8 images in Bari, Italy. *International*
680 *Journal of Remote Sensing*, 36(19-20), 4820-4835. DOI:
681 10.1080/01431161.2015.1070325
- 682 Shearer, A. W., Mouat, D. A., Bassett, S. D., Binford, M. W., Johnson, C. W., & Saarinen, J.
683 A. (2006). Examining development-related uncertainties for environmental
684 management: Strategic planning scenarios in Southern California. *Landscape and*
685 *Urban Planning*, 77(4), 359-381. DOI: 10.1016/j.landurbplan.2005.04.005
- 686 Shan, J., & Sampath, A. (2017). Building extraction from LiDAR point clouds based on
687 clustering techniques. In *Topographic Laser Ranging and Scanning* (pp. 421-444).
688 CRC Press.

- 689 Shufelt, J. A. (1999). Performance evaluation and analysis of monocular building extraction
690 from aerial imagery. *IEEE Transactions on Pattern Analysis and Machine*
691 *Intelligence*, 21(4), 311-326. DOI: 10.1109/34.761262
- 692 Simonetto, E., Oriot, H., Garello, R., & Le Caillec, J. (2003). *Radargrammetric processing*
693 *for 3-D building extraction from high-resolution airborne SAR data*. Paper presented
694 at the INTERNATIONAL GEOSCIENCE AND REMOTE SENSING
695 SYMPOSIUM. DOI: 10.1109/IGARSS.2003.1294320
- 696 Suveg, I., & Vosselman, G. (2004). Reconstruction of 3D building models from aerial images
697 and maps. *ISPRS Journal of Photogrammetry and Remote Sensing*, 58(3), 202-224.
698 DOI:10.1016/j.isprsjprs.2003.09.006
- 699 Tadono, T., Ishida, H., Oda, F., Naito, S., Minakawa, K., & Iwamoto, H. (2014). Precise
700 global DEM generation by ALOS PRISM. *ISPRS Annals of the Photogrammetry,*
701 *Remote Sensing and Spatial Information Sciences*, 2(4), 71. DOI:10.5194/isprsannals-
702 II-4-71-2014
- 703 Thiele, A., Cadario, E., Schulz, K., Thonnessen, U., & Soergel, U. (2007). Building
704 recognition from multi-aspect high-resolution InSAR data in urban areas. *IEEE*
705 *Transactions on Geoscience and Remote Sensing*, 45(11), 3583-3593. DOI:
706 10.1109/TGRS.2007.898440
- 707 Turker, M., & Koc-San, D. (2015). Building extraction from high-resolution optical
708 spaceborne images using the integration of support vector machine (SVM)
709 classification, Hough transformation and perceptual grouping. *International Journal*
710 *of Applied Earth Observation and Geoinformation*, 34, 58-69. DOI:
711 10.1016/j.jag.2014.06.016
- 712 UN DESA. (2015). World population projected to reach 9.7 billion by 2050. In: United
713 Nations Homepage New York.
- 714 UN DESA. (2018). *World Urbanisation Prospects, 2018 Revision*. Retrieved from New York:
- 715 Verma, V., Kumar, R., & Hsu, S. (2006). *3D building detection and modeling from aerial*
716 *LIDAR data*. Paper presented at the Computer Vision and Pattern Recognition, 2006
717 IEEE Computer Society Conference on. DOI: 10.1109/CVPR.2006.12
- 718 Wack, R., & Wimmer, A. (2002). Digital terrain models from airborne laserscanner data-a
719 grid based approach. *International Archives of Photogrammetry Remote Sensing and*
720 *Spatial Information Sciences*, 34(3/B), 293-296.
- 721 Wang, R., Cai, M., Ren, C., Bechtel, B., Xu, Y., & Ng, E. (2019). Detecting multi-temporal
722 land cover change and land surface temperature in Pearl River Delta by adopting
723 local climate zone. *Urban Climate*, 28, 100455. DOI:10.1016/j.uclim.2019.100455

- 724 Wang, R., Ren, C., Xu, Y., Lau, K. K.-L., & Shi, Y. (2018). Mapping the local climate zones
725 of urban areas by GIS-based and WUDAPT methods: A case study of Hong Kong.
726 *Urban Climate*, 24, 567-576. DOI:10.1016/j.uclim.2017.10.001
- 727 Wegner, J. D., Ziehn, J. R., & Soergel, U. (2010). *Building detection and height estimation*
728 *from high-resolution InSAR and optical data*. Paper presented at the Geoscience and
729 Remote Sensing Symposium (IGARSS), 2010 IEEE International. DOI:
730 10.1109/IGARSS.2010.5653386
- 731 Weidner, U., & Förstner, W. (1995). Towards automatic building extraction from high-
732 resolution digital elevation models. *ISPRS journal of Photogrammetry and Remote*
733 *Sensing*, 50(4), 38-49. DOI: 10.1016/0924-2716(95)98236-S
- 734 Wong, N. H., Jusuf, S. K., Syafii, N. I., Chen, Y., Hajadi, N., Sathyanarayanan, H., &
735 Manickavasagam, Y. V. (2011). Evaluation of the impact of the surrounding urban
736 morphology on building energy consumption. *Solar Energy*, 85(1), 57-71. DOI:
737 10.1016/j.solener.2010.11.002
- 738 Xu, Y., Ren, C., Ma, P., Ho, J., Wang, W., Lau, K. K.-L., . . . Ng, E. (2017a). Urban
739 morphology detection and computation for urban climate research. *Landscape and*
740 *Urban Planning*, 167, 212-224. DOI: 10.1016/j.landurbplan.2017.06.018
- 741 Xu, Y., Ren, C., Ma, P., Ho, J., Wang, W., Lau, K. K.-L., . . . Ng, E. (2017b). Urban
742 morphology detection and computation for urban climate research. *Landscape and*
743 *Urban Planning*, 167(Supplement C), 212-224.
744 DOI:10.1016/j.landurbplan.2017.06.018
- 745 Yin, L., & Wang, Z. (2016). Measuring visual enclosure for street walkability: Using machine
746 learning algorithms and Google Street View imagery. *Applied Geography*, 76, 147-
747 153. DOI: 10.1016/j.apgeog.2016.09.024
- 748 Yu, B., Liu, H., Wu, J., & Lin, W.-M. (2009). Investigating impacts of urban morphology on
749 spatio-temporal variations of solar radiation with airborne LIDAR data and a solar
750 flux model: a case study of downtown Houston. *International Journal of Remote*
751 *Sensing*, 30(17), 4359-4385. DOI: 10.1080/01431160802555846
- 752 Zeng, L., Lu, J., Li, W., & Li, Y. (2018). A fast approach for large-scale Sky View Factor
753 estimation using street view images. *Building and Environment*, 135, 74-84. DOI:
754 10.1016/j.buildenv.2018.03.009
- 755 Zhan, Q., Meng, F., & Xiao, Y. (2015). Exploring the relationships of between land surface
756 temperature, ground coverage ratio and building volume density in an urbanized
757 environment. *The International Archives of Photogrammetry, Remote Sensing and*
758 *Spatial Information Sciences*, 40(7), 255. DOI: 10.5194/isprsarchives-XL-7-W3-255-
759 2015

760 Zhou, Q.-Y., & Neumann, U. (2008). *Fast and extensible building modeling from airborne*
761 *LiDAR data*. Paper presented at the Proceedings of the 16th ACM SIGSPATIAL
762 international conference on Advances in geographic information systems. DOI:
763 10.1145/1463434.1463444

764 **Developing a rapid method of 3-dimensional urban**
765 **morphology extraction using open-source data**

766 **- Supplementary materials -**

767

768 *Chao REN^a, Meng CAI^{b*}, Xinwei LI^a, Yuan SHI^b, Linda See^c*

769 ^aFaculty of Architecture, The University of Hong Kong

770 ^bSchool of Architecture, The Chinese University of Hong Kong, Shatin, N.T.,
771 Hong Kong S.A.R., China

772 ^cInternational Institute for Applied Systems Analysis (IIASA), Laxenburg,
773 Austria

774

775 The corresponding author's* email addresses: caimeng@link.cuhk.edu.hk

776 Phone: +852-64870834

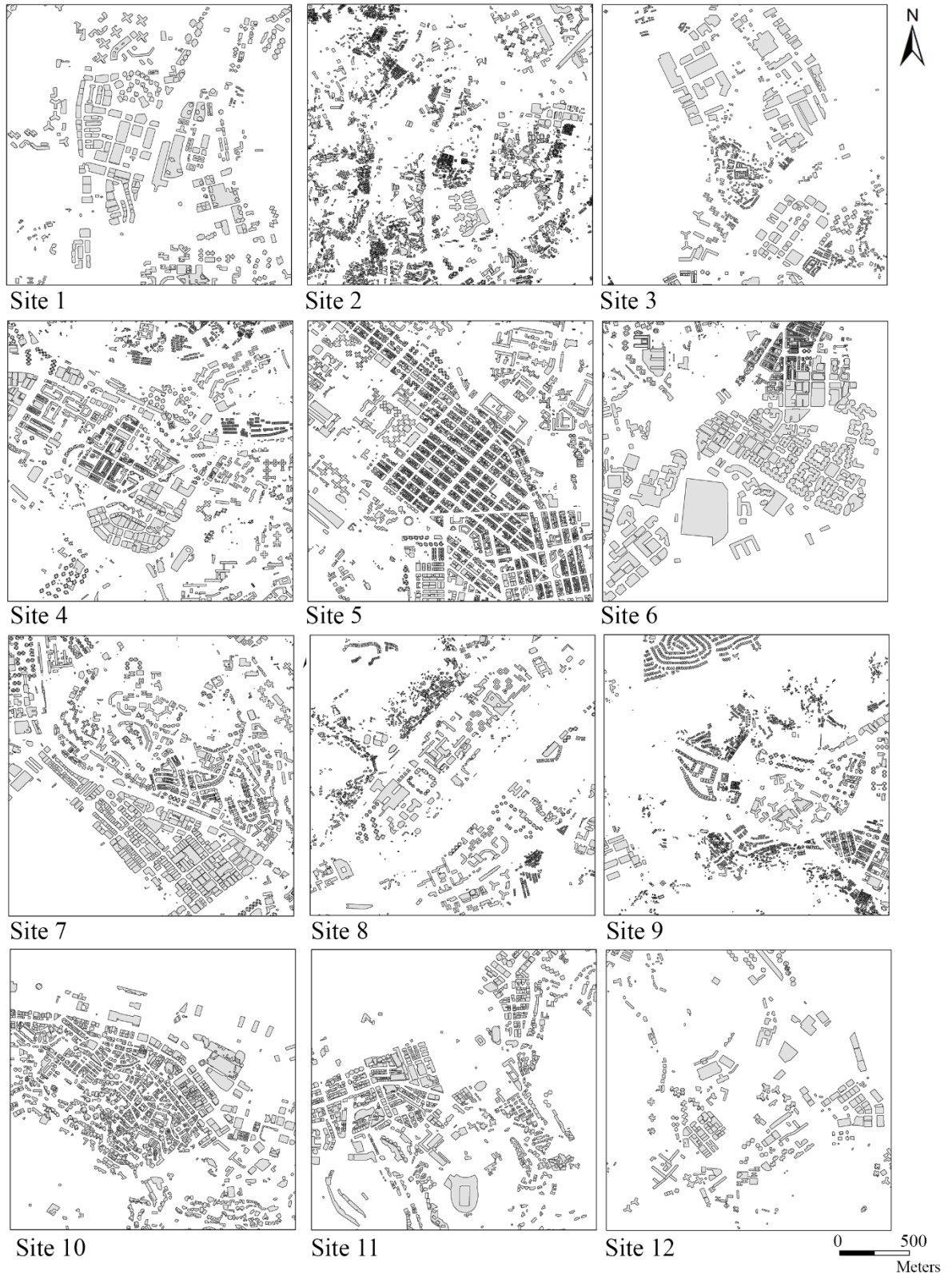
777 Postal addresses: Rm 505, AIT Bldg, School of Architecture, The Chinese
778 University of Hong Kong, Shatin, New Territories, Hong Kong SAR

779

780

781 An example of the URL to retrieve the styled map is:
782 https://maps.googleapis.com/maps/api/staticmap?key=YOUR_API_KEY¢er=22.32,114.16&zoom=17&format=png32&maptypes=roadmap&style=element:labels%7Cvisibility:off&style=feature:administrative%7Cvisibility:off&style=feature:administrative.land_parcel%7Cvisibility:off&style=feature:administrative.neighborhood%7Cvisibility:off&style=feature:landscape.man_made%7Celement:geometry.fill%7Ccolor:0xffff%7Cvisibility:on&style=feature:landscape.man_made%7Celement:geometry.stroke%7Ccolor:0x000000%7Cvisibility:on&style=feature:landscape.natural%7Cvisibility:off&style=feature:landscape.natural%7Celement:geometry.stroke%7Ccolor:0x000000%7Cvisibility:on&style=feature:poi%7Ccolor:0x000000&style=feature:poi%7Celement:geometry.fill%7Ccolor:0xffff%7Cvisibility:on%7Cweight:3.5&style=feature:poi%7Celement:geometry.stroke%7Ccolor:0x000000&style=feature:poi.park%7Cvisibility:off&style=feature:road%7Cvisibility:off&style=feature:transit%7Cvisibility:off&style=feature:water%7Cvisibility:off&size=640x640.

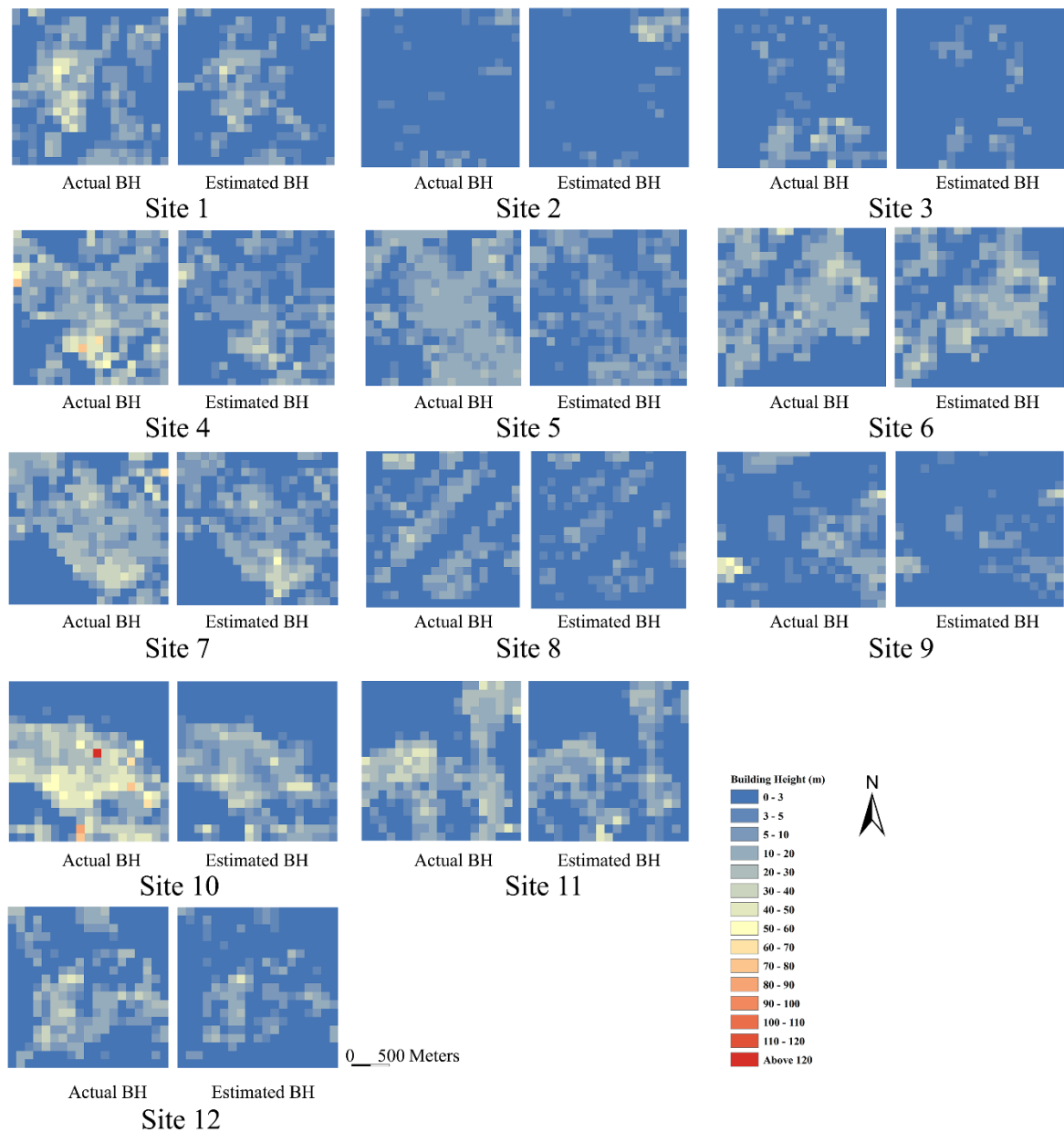
795



796

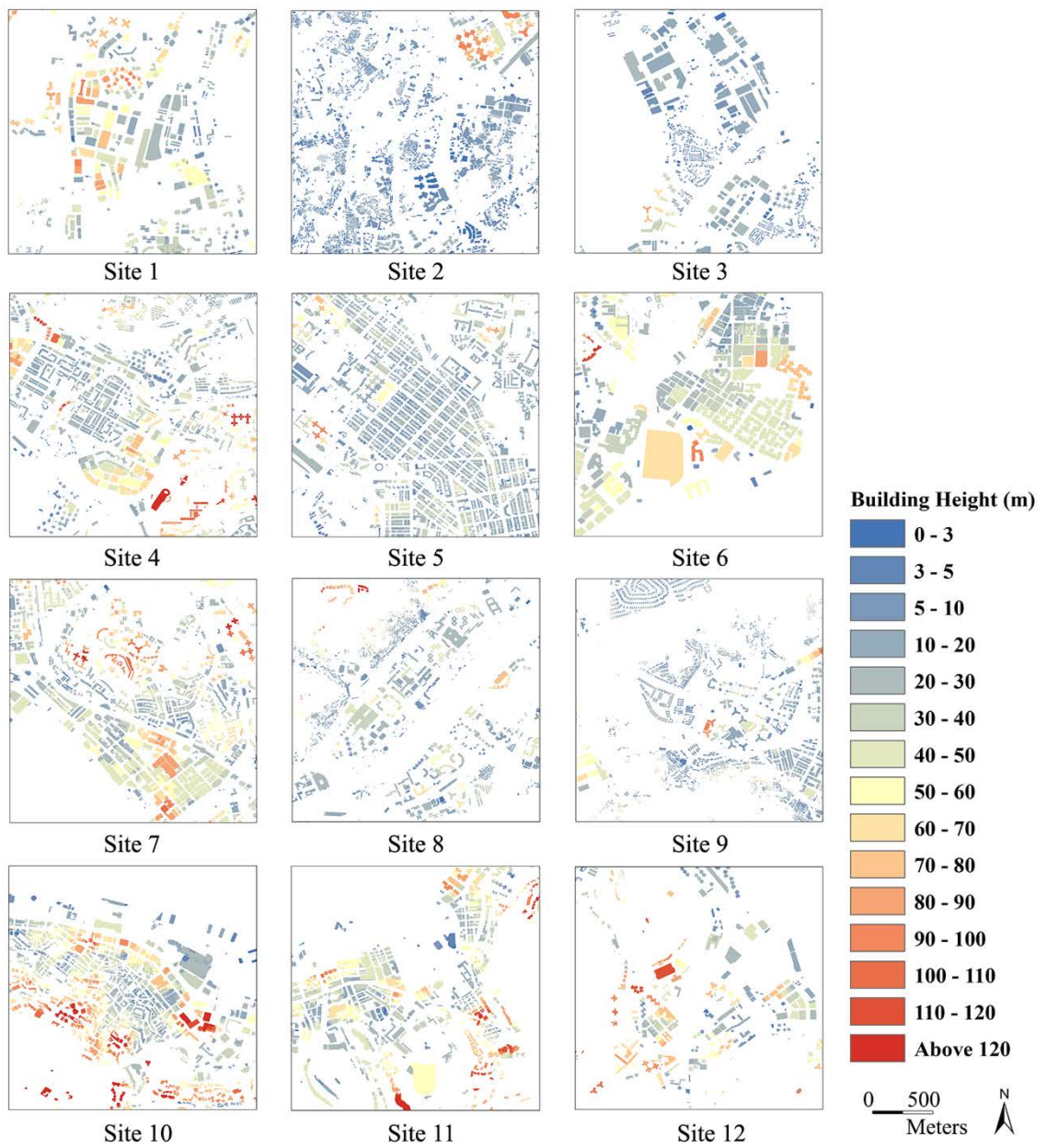
797 **Figure S1.** Building footprint extraction for all 12 selected sites.

798



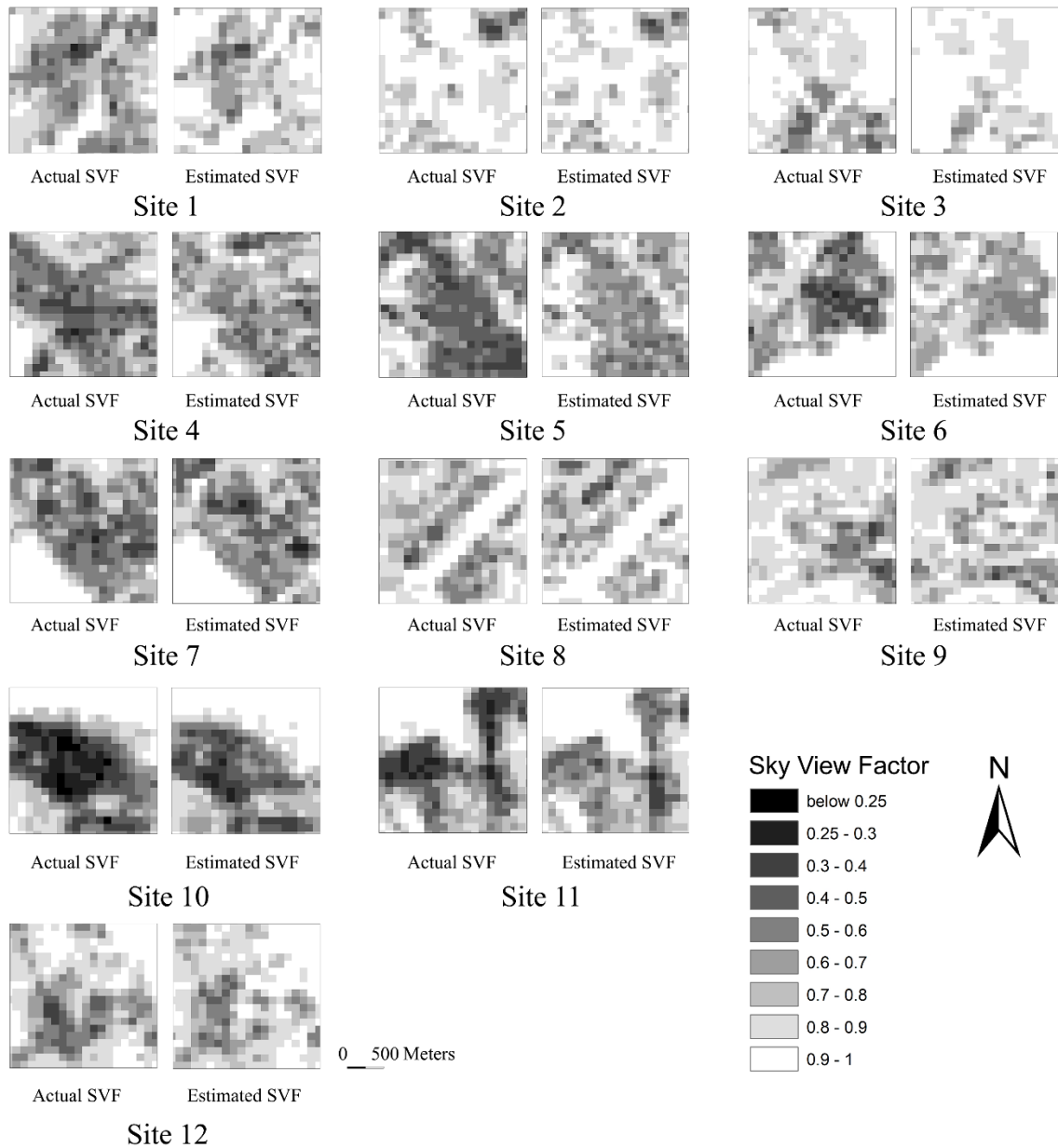
799

800 **Figure S2.** The actual building height and estimated building height of all 12 sites at a
 801 100m grid resolution.



802

803 **Figure S3.** The estimated building height of all 12 sites.



804

805 **Figure S4.** The actual SVF and estimated SVF of all 12 sites at a 100m grid
 806 resolution.